Ray-Chaotic Footprints in Deterministic Wave Dynamics: A Test Model With Coupled Floquet-Type and Ducted-Type Mode Characteristics

Giuseppe Castaldi, Vincenzo Fiumara, Vincenzo Galdi, *Senior Member, IEEE*, Vincenzo Pierro, Innocenzo M. Pinto, *Member, IEEE*, and Leopold B. Felsen, *Life Fellow, IEEE*

***Abstract*—Ray chaos, manifested by the exponential divergence of trajectories in an originally thin ray bundle, can occur even in *linear* electromagnetic propagation environments, due to the inherent *nonlinearity* of *ray-tracing* maps. In this paper, we present a novel (two-dimensional) test example of such an environment which embodies intimately coupled refractive wave-trapping and periodicity-induced multiple scattering phenomenologies, and which is amenable to *explicit full-wave* analysis. Though strictly nonchaotic, it is demonstrated that under appropriate conditions which are inferred from a comprehensive parametric database generated via the above-noted rigorous reference solution, the high-frequency wave dynamics exhibits trends toward irregularity and other peculiar characteristics; these features can be interpreted as "ray-chaotic footprints," and they are usually not observed in geometries characterized by "regular" ray behavior. In this connection, known analogies from other disciplines (particularly quantum physics) are briefly reviewed and related to the proposed test configuration. Moreover, theoretical implications and open issues are discussed, and potential applications are conjectured.**

***Index Terms*—Ducted-type modes, Floquet theory, ray chaos.**

I. Introduction

FIRST envisaged, in connection with celestial mechanics, by the French mathematician Poincaré [1] in the late nineteenth century, and subsequently brought to formal completion by the Russian school (see, e.g., [2]–[5]), deterministic chaos has gradually emerged as an ubiquitous natural phenomenon with a wealth of pervasive and intriguing theoretical implications. During the last few decades, its relevance in all fields of applied science and engineering has been recognized (see, e.g., [6]), as evidenced by the steadily increasing topical literature (see, e.g., the bibliography database maintained by the Nonlinear Dynamics Group at the Johannes Gutenberg University of Mainz, Germany [7]). In essence, deterministic chaos is manifested by exponentially increasing separation between originally nearby phase-space trajectories that describe the evolution of an even feebly nonlinear dynamical system with sufficiently many degrees of freedom; this leads to long-time algorithmic unpredictability and random-like behavior. The reader is referred to classic textbooks and review articles such as [8]–[13] for introduction and review concerning this subject area.

Electromagnetic (EM) chaos has so far elicited relatively little attention within the applied EM community (see [14] for a compact review). Conceivable EM chaotic scenarios are those where chaos stems from *circuit* nonlinearities (e.g., an antenna, or a transmission line, loaded by a Chua double-scroll circuit [15]) or from nonlinear *material* constitutive properties [16], as well as those where chaos can occur in *linear* media due to *nonlinear coupling* between mechanical and EM degrees of freedom (e.g., in Fabry–Perot resonators with (freely swinging, heavy) pendular mirrors [17]). However, much more intriguing is the class of EM boundary value problems (BVPs) that tend toward *ray chaos* (i.e., eventual *exponentially* diverging sensitivity to initial conditions) in smoothly varying *linear* EM propagation environments. In such environments, ray-chaotic trends can be induced by certain geometrical features, e.g., concave portions of a boundary that can support very many multiple reflections, which are reinforced through appropriate refractive (focusing) confinement in the ambient medium. In this connection, it is instructive to examine formal analogies between ray optics and classical particle mechanics like the Sinai [18] (rectangular cavity with circular intrusion) or Bunimovich [19] (stadium-shaped) chaotic "billiards" in *internal* BVPs, or the "n-disk pinball" ($n \geq 3$) scenarios in *external* BVPs [20], [21]. Also relevant are perspectives originated within the framework of quantum physics, the so-called *wave/quantum chaology*, pertaining to classical versus quantum chaos (see [22]–[25] for a review). Critical in the assessment of ray chaos in deterministic linear smoothly configured propagation environments is the *inherent nonlinearity* of *ray-tracing* maps [governed by the nonlinear eikonal equation $(\nabla\varphi)^2 = n^2$, where φ is the ray phase and n is the (inhomogeneous) refractive index] which evolve from successive ray-impact points. This introduces into the high-frequency (HF) asymptotic *wave* field tracking of solutions of a *linear* wave equation via uniformized ray theory, which does not exhibit *inherent* exponential sensitivity to initial conditions for *nonvanishing* wavelengths, an artifact attributable to the *zero-wavelength-limit* model with its *nonlinear* properties. At any small but *finite* wavelength, the wavelength sets a scale beyond which "complexity" cannot be further resolved. There is

Manuscript received November 10, 2003; revised May 3, 2004. The work of L. B. Felsen was supported in part by Polytechnic University, Brooklyn, NY.

G. Castaldi, V. Galdi, V. Pierro, and I. M. Pinto are with the Waves Group, Department of Engineering, University of Sannio, I-82100 Benevento, Italy (e-mail: castaldi@unisannio.it; vgaldi@unisannio.it; pierro@unisannio.it; pinto@sa.infn.it).

V. Fiumara is with the Department of Electrical and Information Engineering, University of Salerno, I-84084 Fisciano (SA), Italy (e-mail: vfiumara@unisa.it).

L. B. Felsen is with the Department of Electrical and Computer Engineering, Polytechnic University, Brooklyn, NY 11201 USA and also with the Department of Aerospace and Mechanical Engineering, Boston University, Boston, MA 02215 USA (e-mail: lfelsen@bu.edu).

Digital Object Identifier 10.1109/TAP.2004.841296

substantiated evidence that *ray-chaotically inclined* BVPs in the short (but finite) wavelength regime exhibit "ray-chaotic footprints" in irregular-appearing wave-dynamical signatures which differ substantially from those associated with BVPs exhibiting "regular" ray behavior. Thus, the onset of ray chaos in ray-chaotically inclined BVPs is an incisive diagnostic *indicator* of the need to look for alternative modeling of the phenomenology, just as the "catastrophies" near caustics in nonuniform ray theory are an indicator of the need for uniformization.

Ray chaos has already been demonstrated to play a key role in certain EM applications, including characterization of complex radar signatures [26]–[28] and of reverberating enclosures [29], [30], as well as design of high-performance optical devices [31], [32]. Our intent in this paper is to gain deeper insights into the wave-physical mechanisms that govern the tendency toward, and the onset of, ray-chaotic footprints in ray-chaotically inclined regular-appearing EM propagation and scattering environments. To this end, we introduce and explore a *novel synthetic complex* test model configuration comprised of a smoothly varying deterministic ambient medium above a perfectly conducting smooth undulating boundary that establishes strong coupling between refractive wave-trapping and Floquet-type periodicity-induced boundary-multiple-scattering phenomenologies ("complexity" here should be interpreted in its broadest sense, implying that "the whole is more than the sum of its parts," so that reductionistic approaches are not applicable [33]). Remarkably, this truly complex (though apparently simple) test environment is amenable to rigorous explicit full-wave analysis. A numerical database constructed from this analysis has allowed parametric studies, which serve as reference solutions for establishing conditions that favor the onset of ray-chaotic footprints. Known results and models from *wave chaology* are introduced in EM-familiar terminology and utilized when appropriate.

The rest of this paper is laid out as follows. Section II contains the proposed model test configuration and the problem formulation. Section III deals with its ray-chaotic behavior, and Section IV with the proposed full-wave analysis. The comprehensive parametric analysis of the wave dynamics, highlighting possible ray-chaotic footprints and validated by the numerical database, is presented in Section V, with brief discussion of potential applications. Conclusions and open issues are discussed in Section VI.

II. Problem Formulation

The test configuration was first explored in [34] and is illustrated in Fig. 1. All fields and geometries are two-dimensional (2-D) in the y-independent (x, z) space. The structure involves a grating consisting of a smooth perfectly conducting periodic undulating surface with profile $z = \zeta(x)$, having peak-to-peak height Δ and period a. The medium above the surface is a dielectric layer of thickness h with exponentially tapered refractive index profile, which is vacuum-matched at the top interface $z = 0$ and reaches its maximum value n_h at $z = -h$

$$n(z) = \exp\left(\frac{\gamma z}{2}\right), \quad \gamma = -\frac{2}{h}\log n_h. \tag{1}$$

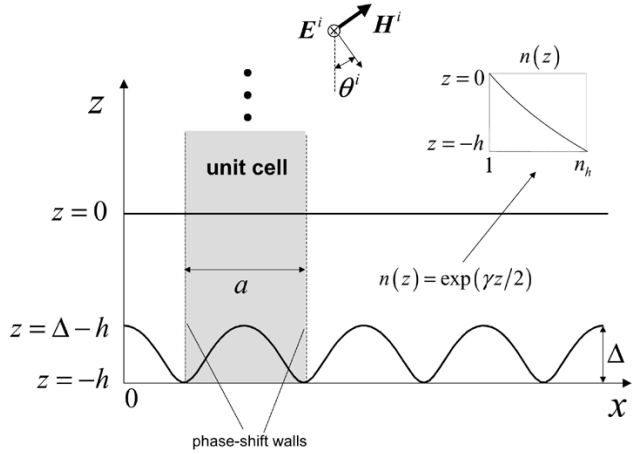

Fig. 1. Problem schematic: A perfectly conducting undulating surface with peak-to-peak height Δ and spatial period a is topped by a dielectric slab with thickness h. The refractive index of the dielectric layer is vacuum-matched at $z = 0$ and grows exponentially with depth up to a value n_h at $z = -h$ (see inset). Also shown are the TE-polarized plane-wave excitation (with incidence angle θ^i and y-directed electric field) and the unit cell waveguide (with phase-shift walls) utilized in the full-wave analysis in Section IV.

The undulating profile has the form

$$\zeta(x) = \bar{z} + \frac{2}{\gamma}\log\left[1 + b\cos\left(\frac{2\pi}{a}x\right)\right], \quad 0 < b < 1 \tag{2}$$

which is matched to the refractive index profile in (1) through the parameter γ. The implications of this choice for the construction of an explicit tractable full-wave analysis, which will serve as the *reference* solution for subsequent parametric numerical experiments, will be made evident in Section IV. The two parameters $\bar{z}$ and b in (2) can be related to the dielectric layer thickness h, its maximum relative refraction index n_h, and the undulating surface profile height Δ by enforcing the conditions (see Fig. 1) $\zeta(0) = -h + \Delta$, and $\zeta(a/2) = -h$. One thus obtains

$$b = \frac{n_h^{(\Delta/h)} - 1}{n_h^{(\Delta/h)} + 1}, \quad \bar{z} = -h\left[1 - \frac{\log\left(\frac{2n_h^{(\Delta/h)}}{1+n_h^{(\Delta/h)}}\right)}{\log n_h}\right]. \tag{3}$$

Although simple in appearance, this overall configuration may exhibit ray-chaotic behavior over a broad range of parameters (see Section III), accompanied by fairly complex full-wave propagation/scattering characteristics. In comparison with the mechanical analogy of spatially confined typical chaotic billiards, the test configuration differs in two important elements: i) its internal/external access, allowing both confined and leaky modes as well as trapped and reflected ray fields; and ii) the essential role of the wave-trapping refractive index profile in providing the conditions for ray chaos (in this connection, the ray paths for this configuration resemble the trajectories of a heavy point-particle bouncing onto a perfectly elastic, periodically undulating wall [35]; in our case, the exponentially tapered refractive index plays the role of gravity, bending the ray trajectories downward toward the undulating surface).

III. Ray Analysis

A. Ray Tracing

For an unbounded medium with refractive index profile as in (1), integration of the ray equation [36]

$$\frac{d}{ds}\left(n\frac{d\mathbf{r}}{ds}\right)=\nabla n,\quad \left|\frac{d\mathbf{r}}{ds}\right|^2=1 \tag{4}$$

yields, after some algebra, closed-form parametric equations for the ray trajectories, shown in (5) at the bottom of the page. In (4) and (5), s represents the ray parameter (distance along the ray), the arctangent is defined in the interval $[-\pi,\pi]$, and ξ_{0_x}, ξ_{0_z} are the (initial) direction cosines

$$\xi_{0_x}=\left.\frac{dx}{ds}\right|_{s=0},\quad \xi_{0_z}=\left.\frac{dz}{ds}\right|_{s=0},\quad \xi_{0_x}^2+\xi_{0_z}^2=1. \tag{6}$$

The trajectory in (5) is completely specified by assigning the starting point (x_0,z_0) and the initial direction (ξ_{0x},ξ_{0z}). It is easily verified that the trajectory is a downward convex unimodal ($\bigcap$-shaped) curve with vertical asymptotes at

$$\begin{cases} x_{\infty 1}=x_0+\frac{4\mathrm{sgn}(\xi_{0x})}{\gamma}\arctan\left(\sqrt{\frac{1-\xi_{0z}}{1+\xi_{0z}}}\right)\\ x_{\infty 2}=x_0-\frac{4\mathrm{sgn}(\xi_{0x})}{\gamma}\left[\frac{\pi}{2}-\arctan\left(\sqrt{\frac{1-\xi_{0z}}{1+\xi_{0z}}}\right)\right]. \end{cases} \tag{7}$$

The turning point (x_t,z_t) is obtained by enforcing $dz/ds=0$, which yields

$$\begin{cases} x_t=x_0-\frac{4\mathrm{sgn}(\xi_{0x})}{\gamma}\left[\frac{\pi}{4}-\arctan\left(\sqrt{\frac{1-\xi_{0z}}{1+\xi_{0z}}}\right)\right]\\ z_t=z_0+\frac{1}{\gamma}\log\left(1-\xi_{0z}^2\right). \end{cases} \tag{8}$$

Incidentally, the Taylor series expansion (in s) of the trajectory in (5) coincides (up to the first order for x and up to the second order for z) with the ballistic trajectory in its gravitational billiard counterpart [35].

For the configuration of Fig. 1, the ray trajectory (5) can be used only in the dielectric layer region $\zeta(x)<z<0$. Ray interactions with the conducting boundary $\zeta(x)$ in (2), as well as those with the free-space interface at $z=0$, need to be tracked separately, using standard geometrical optics (Snell's laws). In our ray-tracing simulations, the algorithm is initialized by injecting a downward-directed ray at the free-space interface $z=0$, with incidence abscissa $x=x^i$ and incidence angle θ^i (see Fig. 1). The ray trajectory is then evolved via (5), with initial parameters

$$(x_0,z_0)=(x^i,0),\quad (\xi_{0x},\xi_{0z})=(\sin\theta^i,-\cos\theta^i) \tag{9}$$

until it reaches the conducting boundary. Here, the ray impact point and direction are computed by solving the arising nonlinear system of equations [(2) with (5)] numerically [37]; the corresponding reflected ray direction is obtained trivially via specular reflection. The process is iterated, using, instead of (9), each computed impact point and reflection direction as new initial conditions in (5). The ray trajectory thus evolves as a sequence of $\bigcap$-shaped arcs, and remains trapped within the layer until the turning point in (8) lies beyond the free-space interface ($z_t>0$). When this happens, the evolution is stopped, and the exit angle

$$\theta^e\equiv\arcsin\left(\left.\frac{dx}{ds}\right|_{z=0}\right) \tag{10}$$

is recorded.

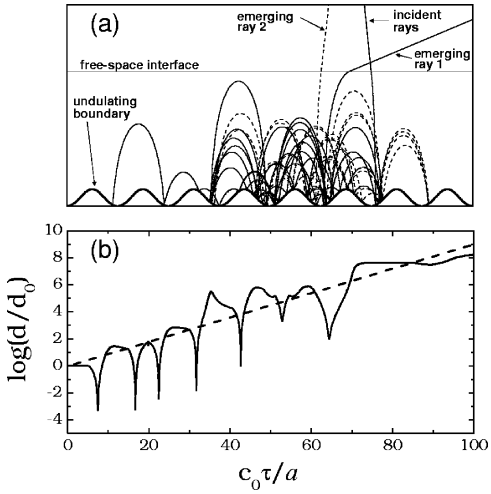

Fig. 2. Geometry as in Fig. 1, with $a=h=1$ (arbitrary units), $\Delta/a=2/(5\pi)$, $n_h=15$, and $\theta^i=15^\circ$. Ray tracing results. (a) Two typical multihop paths originating from nearby incidence points (initial separation $d_0=10^{-3}\cdot a$) display rapidly increasing separation and eventually emerge with widely different exit positions and angles. (b) Separation d between nearby-incident rays (scaled by its initial value d_0) as a function of the "ray time" τ in (11) (scaled by $c_0^{-1}a$). The semi-log scale in the graph, and the dashed linear fit, highlight the *exponential* trend typical of chaotic dynamics.

B. Results From Ray Analysis

We now illustrate some representative results from a comprehensive series of ray-tracing simulations. Fig. 2(a) shows a typical evolution of two multihop ray paths originating from closely adjacent incidence points with initial separation $d_0=10^{-3}\cdot a$ [not resolved in Fig. 2(a)] and with identical incidence angles ($\theta^i=15^\circ$); other parameters are specified in the figure caption. The two initially indistinguishable ray trajectories undergo rapidly *increasing* separation on their travel through the structure, resulting in widely separated exit angles and positions. For the same configuration, Fig. 2(b) shows the logarithm of the ray separation d (in units of its initial value d_0) as a function of the "ray-time"

$$\tau=c_0^{-1}\int_{\text{ray path}} n(s)ds \tag{11}$$

$$\begin{cases} x(s)=x_0-\frac{4\mathrm{sgn}(\xi_{0x})}{\gamma}\left[\arctan\left(\exp\left(-\gamma\frac{s}{2}\right)\sqrt{\frac{1-\xi_{0z}}{1+\xi_{0z}}}\right)-\arctan\left(\sqrt{\frac{1-\xi_{0z}}{1+\xi_{0z}}}\right)\right]\\ z(s)=z_0+s-\frac{2}{\gamma}\log\left[\frac{2}{(1+\xi_{0z})+\exp(-\gamma s)(1-\xi_{0z})}\right] \end{cases} \tag{5}$$

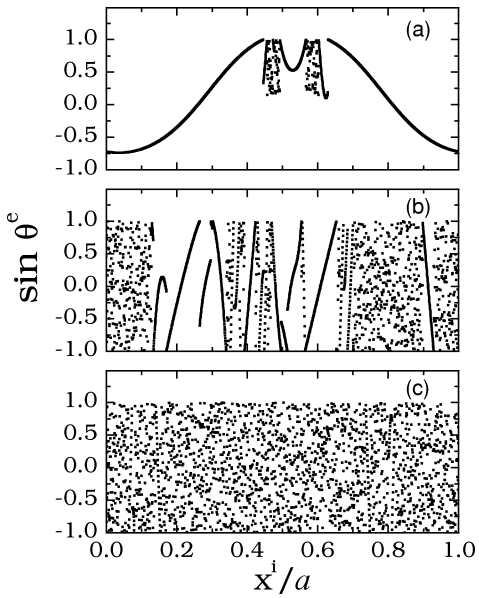

Fig. 3. Geometry as in Fig. 1, with $a = h = 1$ (arbitrary units), $\Delta/a = 2/(5\pi)$, and $\theta^i = 15°$. Sine of ray exit-angle θ^e versus scaled incidence abscissa x^i/a for various values of n_h. (a) $n_h = 1.4$; (b) $n_h = 15$; (c) $n_h = 90$.

with c_0 denoting the free-space wavespeed. With the semi-log scale used in the graph, the linear *exponential* trend (typical of chaotic dynamics) can readily be discerned. Similar trends were observed within a broad range of incidence angles. Note that the slope of the linear fit in Fig. 2(b), averaged over the range of initial conditions, provides an estimate of the "ray-dynamical" Lyapounov exponent [8]–[13]. To provide a compact visualization of regular versus irregular ray behavior, we show in Fig. 3 the sine of the exit angle θ^e in (10) versus the scaled incidence impact point abscissa x^i/a, for a fixed incidence angle and three representative values of the maximum refraction index n_h. One observes intermingled intervals of regular/irregular dependence of the exit angle on the incidence point position in the unit cell. The ray picture in Fig. 2(a) suggests that the irregular behavior stems from long trapping of the ray in the structure before escaping. It is thus not surprising to observe that the measure of the incidence-point set corresponding to regular behavior (i.e., rapidly escaping rays) depends on n_h and tends to zero as n_h is increased (see Fig. 3) as a consequence of the resulting more effective ray-trapping mechanism. As exemplified in Fig. 4, for a fixed value of $n_h = 15$, the measure of the above regular sets (i.e., the incidence-point set corresponding to regular behavior) turns out to be almost independent of the incidence angle [compare Figs. 3(a) and 4(a) and 4(b)]. In these synthetic experiments, the distribution of $\sin\theta^e$ turns out to be *almost uniform,* independently of the incidence angle. This is exemplified in Fig. 4(c), which shows the cumulative distribution function (CDF) (here, the CDF is taken as the ratio between the number of rays with $\sin\theta^e$ smaller than the argument value and the total number of rays in the experiment) exhibiting quasilinear trends, for various incidence angles. Moreover, a closer look reveals that the intermingled regular/irregular structure is hidden at *any* scale, i.e., as the incidence-point position moves within *arbitrarily small* intervals at fixed incidence angle $\theta^i = 15°$, as shown in Fig. 5. In typical examples of open ray-chaotic BVPs

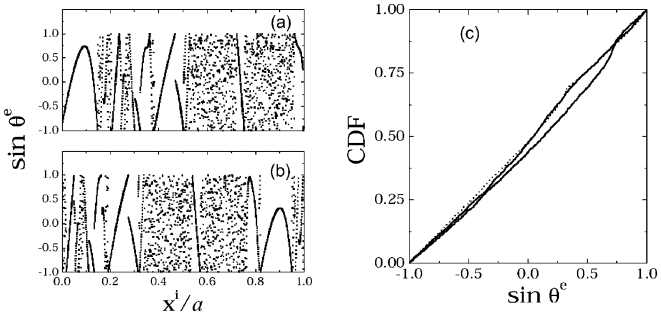

Fig. 4. As in Fig. 3, but for $n_h = 15$ and various incidence angles θ^i. (a), (b) $\theta^i = 45°$ and 75°, respectively. (c) CDF of $\sin\theta^e$, estimated considering 2000 rays with incidence points distributed along the unit cell. — $\theta^i = 15°$; --- $\theta^i = 45°$; ..... $\theta^i = 75°$.

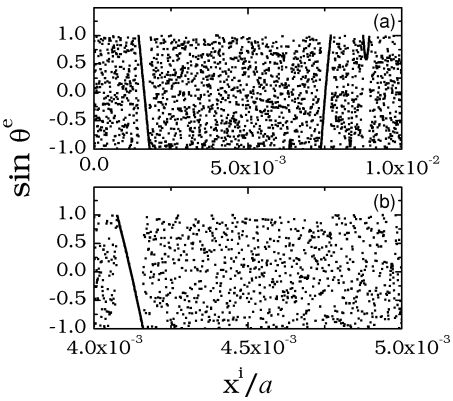

Fig. 5. Magnified details of Fig. 3(b) displaying the intermingled regular/irregular structure at subscales of the unit cell size a. (a) Incidence abscissa $x^i \in [0, a/100]$ (i.e., 1/100 scale) and (b) incidence abscissa $x^i \in [4a/1000, 5a/1000]$ (i.e., 1/1000 scale).

(e.g., the n-disk pinball [20]), the set of irregular ("singular," in the terminology of [20]) points is actually found to have a *fractal* character. In these scenarios, important insight is obtained from the statistical analysis of the "dwell time" (i.e., the time spent by the rays in the structure before escaping) [20]. For our configuration, the dwell time is thus defined as

$$\tau_D = c_0^{-1} \int_{z(s)<0} n(s) ds. \tag{12}$$

Fig. 6 shows the dwell-time complementary CDF for our system with the same parameter configurations as in Fig. 3. In Fig. 6(c) $(n_h = 90)$, a linear *exponential* behavior is observed, irrespective of the incidence angle, as evidenced by the inset plot in semi-log scale. This observation is consistent with the results available in the technical literature [20], from which the dwell-time probability density function $P(\tau_D)$ for strongly chaotic dynamics is known to have the form

$$P(\tau_D) = \gamma_D \exp(-\gamma_D \tau_D) \tag{13}$$

where $\gamma_D = (1 - d_H)\lambda_l$, with λ_l being the Lyapounov exponent associated with the ray dynamics and d_H denoting the Hausdorff dimension of the set of "singular" points [20]. In Fig. 6(a) and (b) ($n_h = 1.4$ and $n_h = 15$, respectively), corresponding to configurations where regions of regular behavior are nonnegligible or even dominant, one still observes an *exponential tail* in the dwell-time complementary CDF. Here, the regular dynamics

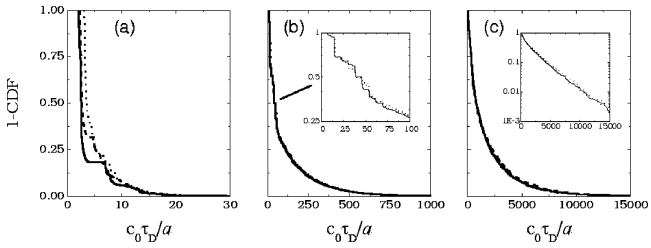

Fig. 6. Complementary CDF (i.e., 1-CDF) of dwell time τ_D in (12) (scaled by $c_0^{-1}a$) for the parameter configurations in Fig. 3, at various values of incidence angle θ^i, estimated considering N_r ray trajectories with incidence abscissa x^i uniformly distributed over the unit cell. (a) $n_h = 1.4$, $N_r = 10^6$; (b) $n_h = 15$, $N_r = 10^5$ (the zoom in the inset highlights the initial staircase behavior); (c) $n_h = 90$, $N_r = 10^4$ (the semi-log scale in the inset highlights the linear exponential behavior). — $\theta^i = 15°$;--- $\theta^i = 45°$; ..... $\theta^i = 75°$.

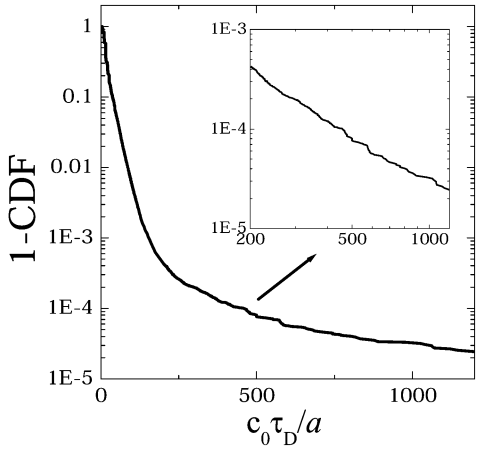

Fig. 7. As in Fig. 6, but with $n_h = 5, \theta^i = 45°$, and $N_r = 10^6$. The semi-log scale in the plot highlights the departure in the tail from linear exponential behavior. The the power-law character of the tail ($\sim \tau_D^{-1.85}$, from numerical fit) is evidenced by the inset plot in log-log scale.

principally affects the initial part of the distribution, with the presence of a *staircase behavior* [clearly evident in Fig. 6(a), and evidenced by the zoom in the inset of Fig. 6(b)]. This behavior can be explained by recalling that regular dynamics here is typically associated with rapidly escaping rays whose dwell times cluster around certain values. From the technical literature (see, e.g., [38] and the references therein), the dwell-time distribution in these mixed cases is expected to exhibit a *power-law* tail, attributed here to long-trapped marginally-stable trajectories. Such a tail, however, was not clearly observed in the above simulations, which are based on sets of 10^5–10^6 trajectory realizations (compatible with our current computational capabilities). Our inability to capture the power-law behavior in these cases may be due to the very small measure of the phase-space islands corresponding to long-trapped marginally stable trajectories, which are very difficult to sample numerically in the absence of precise a priori knowledge of the ray dynamics. To gain such precise knowledge would require a parametric analysis, which is beyond the scope of this preliminary investigation. An example parameter configuration ($n_h = 5$, $\theta^i = 45°$) where the power-law tail was clearly observed is shown in Fig. 7. The semi-log scale in the plot highlights the departure in the tail from linear exponential behavior. The power-law behavior of the tail is evidenced in the log-log scale inset plot, and was estimated numerically (via curve fitting) to be $\sim \tau_D^{-1.85}$, which is consistent with observations in the technical literature (see, e.g., [38] and the references therein).

To sum up, the above-noted features tend to indicate that the ray dynamics in our system is generally of "mixed" type [12], [24], with the presence of both *regular* and *chaotic* regions in the phase space. However, it seems possible to tune the parameter configuration (e.g., acting on the refractive index gradient) so as to render the dynamics *strongly chaotic*.

Concerning the philosophical question as to the accuracy of our (or *any*) computer simulation due to unavoidable roundoff errors, our ray simulation results might appear questionable. Chaos implies exponential amplification of small differences, which can *always* be expected to lead to exponential divergence of a *numerical* (i.e., finite-precision) trajectory from the *true* trajectory with the same initial conditions. This fundamental issue has been investigated in the topical literature (see, e.g., [12] and [39]), and the reassuring conclusion is that a *numerical* trajectory *is* meaningful since, in its neighborhood, there generally exist a *true* (i.e., errorless) trajectory with slightly different initial conditions.

IV. Full-Wave Analysis

We now turn to the full-wave analysis of the scattering and propagation behavior of the configuration in Fig. 1. We restrict our attention to time-harmonic transverse-electric (TE) plane-wave illumination, with suppressed $\exp(j\omega t)$ dependence

$$E^i(x,z) = E_0 \exp\left[-jk_0(x\sin\theta^i - z\cos\theta^i)\right] \tag{14}$$

where $k_0 = \omega\sqrt{\epsilon_0\mu_0} = 2\pi/\lambda_0$ indicates the free-space wavenumber, with λ_0 denoting the free-space wavelength. To obtain numerical reference solutions for similar classes of problems (like graded-index diffraction gratings), some authors have used semianalytic Floquet-based finite-difference [40] and transmission-matrix [41] methods. We decided to pursue an entirely analytically based problem-matched test model approach tailored around the particular ray-chaotically inclined deterministic propagation environment in Fig. 1, in order a) to have a rigorous anchor for parametric exploration of the evolution of ray-chaotic footprints and b) to hopefully render the corresponding parametric numerical implementations more efficient.

A. Solution Strategy

Referring to Fig. 1, in view of the assumed spatial periodicity of the boundary and the x-invariance of the dielectric, the problem can be reduced to the analysis of a generic unit cell with phase-shift boundary conditions at the lateral walls. Accordingly, the field E^r reflected into the half-space $z > 0$, and the field E^t transmitted into the region $\zeta(x) < z < 0$, may be represented as Floquet expansions

$$E^r(x,z) = E_0 \sum_{m=-\infty}^{\infty} b_m \exp\left[-j(k_{xm}x + k_{0zm}z)\right], \quad z > 0 \tag{15}$$

$$E^t(x,z) = E_0 \sum_{m=-\infty}^{\infty} c_m(z) \exp(-jk_{xm}x), \quad \zeta(x) < z < 0. \tag{16}$$

In (15) and (16), b_m and $c_m(z)$ are unknown mode amplitudes, whereas k_{xm} and k_{0zm} represent the mth Floquet mode transverse and longitudinal wavenumbers, respectively

$$k_{xm} = k_0 \sin\theta^i + m\frac{2\pi}{a}$$
$$k_{0zm} = \sqrt{k_0^2 - k_{xm}^2}, \quad \mathrm{Re}(k_{0zm}) \geq 0. \tag{17}$$

The transmitted field inside the dielectric layer is governed by the Helmholtz equation

$$\left(\frac{\partial^2}{\partial x^2} + \frac{\partial^2}{\partial z^2}\right) E^t(x,z) + k_0^2 n^2(z) E^t(x,z) = 0 \tag{18}$$

which, by inserting the expansion in (16), yields a (simple) countable infinity of second-order ordinary differential equations in the unknown coefficients $c_m(z)$. For the class of refractive index profiles in (1), such equations can be recast in the canonical form

$$\frac{d^2u}{dw^2} + \left(\eta^2 e^{2w} - \nu^2\right) u = 0 \tag{19}$$

where

$$w = \frac{\gamma z}{2}, \quad \eta = \frac{2k_0}{|\gamma|}, \quad \nu^2 = \left(\frac{2k_{xm}}{\gamma}\right)^2. \tag{20}$$

Equation (19) admits solutions in the form $u(w) = \mathcal{C}_\nu[\eta e^w]$, with $\mathcal{C}_\nu$ being a generic Bessel/Hankel function of order ν [42]. Accordingly, the $c_m(z)$ functions in (16) can be expressed as linear combinations of two linearly independent Hankel functions

$$c_m(z) = u_m U_m(z) + v_m V_m(z) \tag{21}$$

$$\left.\begin{matrix} U_m(z) \\ V_m(z) \end{matrix}\right\} = \begin{cases} H^{(1)}_{|(2k_{xm}/\gamma)|}\left[\frac{2k_0}{|\gamma|}\exp\left(\frac{\gamma}{2}z\right)\right] \\ H^{(2)}_{|(2k_{xm}/\gamma)|}\left[\frac{2k_0}{|\gamma|}\exp\left(\frac{\gamma}{2}z\right)\right] \end{cases} \tag{22}$$

thereby reducing the original problem to the calculation of the unknown coefficient sets b_m, u_m, and v_m, via enforcing the boundary conditions at the interfaces $z = 0$ (continuity of the tangential components of the electric and magnetic field) and $z = \zeta(x)$ (vanishing of the tangential component of the electric field)

$$\begin{cases} E^t(x,0^-) = E^r(x,0^+) + E^i(x,0^+) & \text{(23a)} \\ \dfrac{\partial}{\partial z}E^t(x,0^-) = \dfrac{\partial}{\partial z}E^r(x,0^+) + \dfrac{\partial}{\partial z}E^i(x,0^+) & \text{(23b)} \\ E^t(x,\zeta(x)) = 0. & \text{(23c)} \end{cases}$$

From the first set of boundary conditions in (23a) and (23b) at $z = 0$, one obtains a countable infinity of linear equations as shown in (24a) and (24b) at the bottom of the page, where $m = -\infty, \ldots, \infty$, δ_{mn} represents the Kronecker delta, and the overdot denotes differentiation with respect to the argument. Eliminating the b_m coefficients, one further obtains

$$u_m\left[k_{z0m}U_m(0) - jk_0\dot{U}_m(0)\right] = -v_m\left[k_{z0m}V_m(0) - jk_0\dot{V}_m(0)\right] + 2k_{z0m}\delta_{m0}. \tag{25}$$

On the other hand, the boundary condition in (23c) at the conducting undulating surface $z = \zeta(x)$ yields

$$\sum_{m=-\infty}^{\infty} \{u_m U_m[\zeta(x)] + v_m V_m[\zeta(x)]\} \exp\left(-jm\frac{2\pi x}{a}\right) = 0 \tag{26}$$

which is far less straightforward to deal with. Recalling that the functions $U_m[\zeta(x)]$, $V_m[\zeta(x)]$ are x-periodic with period a, it is suggestive to Fourier-expand them so as to recast (26) into a more manageable Fourier series. In this connection, the special class of profiles $\zeta(x)$ in (2) turns out to be particularly "friendly," since it maps the functions $U_m[\zeta(x)]$, $V_m[\zeta(x)]$ into fairly simple canonical forms

$$(U,V)_m[\zeta(x)] = H_\nu^{(1,2)}\left[c' + b'\cos\left(\frac{2\pi}{a}x\right)\right] \tag{27}$$

where [see (22)]

$$\nu = \left|\frac{2}{\gamma}k_{xm}\right|, \quad c' = \frac{2k_0}{|\gamma|}\exp\left(\frac{\gamma\bar{z}}{2}\right)$$
$$b' = \frac{2k_0}{|\gamma|}b\exp\left(\frac{\gamma\bar{z}}{2}\right). \tag{28}$$

The Fourier expansions of (27) can thus be performed analytically, by first utilizing the Neumann addition formula [42]

$$H_\nu^{(1,2)}\left[c' + b'\cos\left(\frac{2\pi}{a}x\right)\right] = \sum_{p=-\infty}^{\infty} H_{\nu-p}^{(1,2)}(c') \times J_p\left[b'\cos\left(\frac{2\pi}{a}x\right)\right] \tag{29}$$

and subsequently Fourier-expanding the J_p Bessel functions in (29)

$$J_p\left[b'\cos\left(\frac{2\pi}{a}x\right)\right] = \sum_{q=-\infty}^{\infty} J_{p,q}\exp\left(jq\frac{2\pi x}{a}\right) \tag{30}$$

where [43]

$$J_{p,q} = \frac{1}{a}\int_{-a/2}^{a/2}\exp\left(-jq\frac{2\pi x}{a}\right)J_p\left(b'\cos\frac{2\pi x}{a}\right)dx = \frac{1}{2}\left[1 + (-1)^{p+q}\right] \times J_{(p-q)/2}\left(\frac{b'}{2}\right)J_{(p+q)/2}\left(\frac{b'}{2}\right). \tag{31}$$

$$\begin{cases} \delta_{m0} + b_m = u_m U_m(0) + v_m V_m(0) & \text{(24a)} \\ k_{0zm}(\delta_{m0} - b_m) = -jk_0\left[u_m\dot{U}_m(0) + v_m\dot{V}_m(0)\right] & \text{(24b)} \end{cases}$$

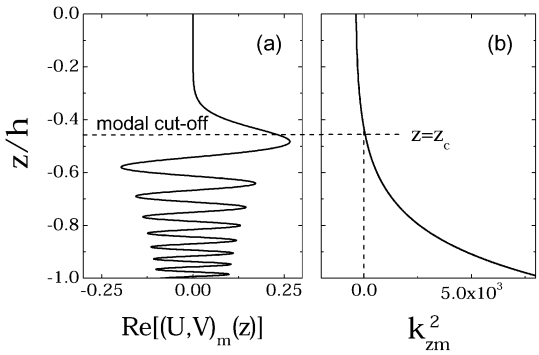

Fig. 8. Typical ducted mode in (36), with $a/\lambda_0 = 6$, $h = a$, $n_h = 15$, $m = 6$, $\theta^i = 15°$. (a) Modal field distribution and (b) modal cutoff condition in (37).

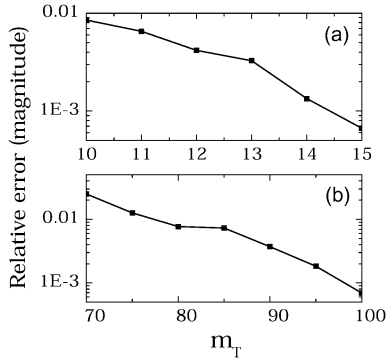

Fig. 9. Geometry as in Fig. 1, with $a = h$, $\Delta/a = 2/(5\pi)$ and $\theta^i = 15°$. Residual truncation-induced error (scaled to incident field amplitude E_0) in boundary conditions (23c) as a function of number of retained modes m_T. (a) $a/\lambda_0 = 0.5$ (low frequency) and (b) $a/\lambda_0 = 6$ (high frequency).

One thus obtains

$$H_\nu^{(1,2)}\left[c' + b'\cos\left(\frac{2\pi x}{a}\right)\right] = \sum_{p=-\infty}^{\infty} H_{\nu-p}^{(1,2)}(c') \times \sum_{q=-\infty}^{\infty} J_{p,q}\exp\left(jq\frac{2\pi x}{a}\right) \quad (32)$$

which can be further recast as

$$H_\nu^{(1,2)}\left[c' + b'\cos\left(\frac{2\pi x}{a}\right)\right] = \sum_{q=-\infty}^{\infty} H_{\nu,q}^{(1,2)} \times \exp\left(jq\frac{2\pi x}{a}\right) \quad (33)$$

where

$$H_{\nu,q}^{(1,2)} = \sum_{p=-\infty}^{\infty} H_{\nu-p}^{(1,2)}(c')J_{p,q}. \quad (34)$$

Substituting (33) into (26) [with (27)], and regrouping the harmonics of the resulting Fourier series, one obtains a countable infinity of linear equations

$$\sum_{m=-\infty}^{+\infty}\left(u_m H_{\nu,p-m}^{(1)} + v_m H_{\nu,p-m}^{(2)}\right) = 0, \quad p = -\infty,\ldots,\infty \quad (35)$$

which, together with (25), can be used to determine the unknown coefficients u_m and v_m, $m = -\infty,\ldots,\infty$.

To better understand the wave phenomenologies involved, we first observe that, in the limit $m \gg 1$, one can verify from (25) that $|u_m| \sim |v_m|$, whence [from (21) and (22)]

$$c_m(z) \sim \mathrm{Re}[(U,V)_m(z)]. \quad (36)$$

Fig. 8(a) shows the typical behavior of (36) in the region $-h < z < 0$. It clearly resembles a *ducted* (longitudinal) mode with the typical oscillatory and evanescent regimes. The two regimes merge into a transition (turning point) region located in the vicinity of $z = z_c$, defined by the modal cutoff condition [36], [44] [see Fig. 8(b)]

$$k_{zm}^2(z_c) \equiv k_0^2 n^2(z_c) - k_{xm}^2 = 0. \quad (37)$$

The wave dynamics of the configuration in Fig. 1 is thus parameterized in terms of Floquet (plane) waves (in free space) and ducted modes (in the dielectric layer), coupled through the boundary conditions.

B. Implementation Details and Numerical Convergence

For computational purposes, the series in (34), as well as the Floquet expansions in (15) and (16) [and hence the systems in (25) and (35)], need to be suitably truncated. For the p-summation in (34), we used a pragmatic criterion (validated a posteriori), truncating the expansion when the magnitude of the first omitted term is below a given threshold ($10^{-16}\times$ the leading term). As typical in mode-matching-type algorithms, the truncation of the Floquet expansions (15) and (16) was pursued by inspection, via monitoring the truncation-induced mismatch error in the (most critical) boundary conditions (23c) within the unit cell. As a rule of thumb, we found that truncating (15) and (16) at

$$|m| \le m_T \sim n_h\frac{a}{\lambda_0} \quad (38)$$

and utilizing the pragmatic truncation criterion stated above for the the summation in (34) usually yields acceptable accuracy. The physical interpretation of the truncation condition in (38) can be gauged from the modal cutoff condition in (37) and consists of neglecting in the transmitted field expansion the ducted modes with cutoff level at sufficient distance from the free-space interface ($z_c < -h$). Using the (large order) asymptotic expansion of the Hankel function [42] in (36), one can show that the neglected modes decay exponentially with m

$$c_m \sim (2\pi\nu)^{-(1/2)}\left(\frac{ek_0 n_h}{\nu|\gamma|}\right)^\nu \sim \exp(-\nu\log\nu) \sim \exp(-m\log m). \quad (39)$$

Inclusion of such modes, besides not necessarily improving the overall accuracy, can even yield the opposite effect by eventually deteriorating the numerical conditioning of the system [45]. Fig. 9 illustrates the convergence behavior for two typical configurations which will be considered below. It is observed that the above truncation criteria yield relative residual errors

in the boundary condition (23c) on the order of 10^{-3}. In this and all simulations that follow, the system in (35) was truncated so that $|p-m| \leq m_T$, and subsequently solved, together with (25), using least square methods [45]. Numerical implementation (25-digit precision) was accomplished using Mathematica [46]. As a further consistency check, power conservation was found to hold with acceptable accuracy (relative error $\sim 10^{-3}$).

The above full-wave strategy, in its present form, allows reliable and relatively time-affordable analysis of parameter configurations with electrical size up to $a/\lambda_0 \sim 6$ and maximum refractive index $n_h \sim 15$.

V. Ray-Chaotic Footprints in the Full-Wave Regime

A. Background

Before investigating possible ray-chaotic footprints embedded within the full-wave reference solution in Section IV, we first refer to some relevant known results (see [22]–[25] for a thorough review and analytic details). "Ray-chaotic footprints" denotes distinctive features in the HF wave dynamics which distinguish ray-chaotic BVPs from those (e.g., coordinate-separable) exhibiting *regular* ray behavior. Remarkably, in most cases such features have *universal* properties. For instance, in internal BVPs, the (asymptotic) neighboring-eigenvalue spacing distribution for regular geometries is known to be Poissonian [24]. For ray-chaotic geometries, instead, the spectral (eigenvalue, eigenfunction) ensemble properties have been found to be intimately related to those of (rather general) *random matrices* [47]–[49]. Other examples of ray-chaotic footprints in internal BVPs are related to field nodal-domain statistics [50]. In external BVPs, on the other hand, signatures of ray chaos have been found in the random-like angular spectrum properties of the scattering matrix and cross-sections, with intriguing connections to the dwell-time distribution of the corresponding ray dynamics [20], [21]. For transient excitation, ray-chaos-induced peculiar behavior has been found in *time-reversal* experiments [51]–[53].

With a few notable exceptions (see, e.g., [54]), what seems to emerge is the presence, in the wave dynamics, of a transition from a regular regime (with smooth dependence on parameter variations) to an irregular regime (with sensitive dependence on parameter variations and ergodic random-like behavior) as the frequency of operation is increased. Incidentally, such strong parametric sensitivity is likewise observed in electrically large real-world complex scatterers (e.g., aircraft [55]). In the irregular regime, the full-wave properties of ray-chaotic systems turn out to be most naturally described in *statistical* terms. For ray-chaotic internal BVPs, a well-established statistical model is based on the assumption that the field at any point is a superposition of a large number of plane waves with fixed wavevector amplitude and uniformly distributed arrival-directions and phases [56]. Considering additional ergodicity assumptions, this yields very general consequences in the wavefield statistics: In an arbitrary spatial domain $\mathcal{D}$ spanning several wavelengths (sufficiently large so as to yield meaningful statistics, and yet sufficiently small so as to reveal possible spatial variations), the wavefield samples will form a zero-average Gaussian ensemble [57], with spatial field correlation exhibiting peculiar (universal)

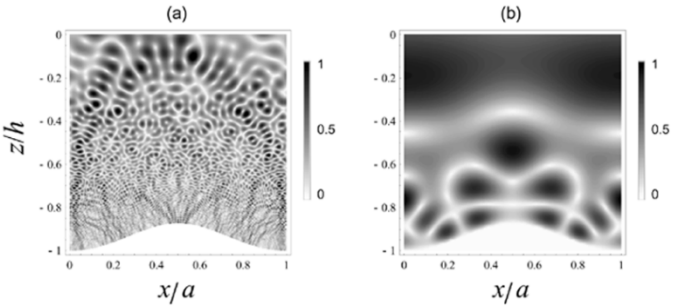

Fig. 10. Parameters as in Fig. 9. Magnitude (grayscale plot) of the transmitted field E^t in (16), normalized with respect to its maximum value $|E^t|_{\max}$, within the unit cell. (a) $a/\lambda_0 = 6$ and (b) $a/\lambda_0 = 0.5$.

forms (e.g., Bessel function J_0 in 2-D cases [56], [58]). The random-plane-wave (RPW) model has been shown to parameterize very well the statistical properties (both predicted [59] and measured [60]) of asymptotic HF wavefunctions of strongly chaotic billiards in the irregular ergodic regime. Interestingly, similar RPW models have been utilized successfully to characterize complex radar signatures [27] as well as narrow-band EM reverberation enclosures [61], [62]. The reader is also referred to [63]–[65], where examples of billiards with "mixed" dynamics are considered and possible deviations from the RPW model are explored.

We now move on to presenting some representative results obtained from the rigorous monochromatic, plane-wave TE-incidence, full-wave analysis in Section IV. In what follows, we consider the geometry in Fig. 1, with $a = h$ and $\Delta/a = 2/(5\pi)$.

B. Our Test Problem: Transmitted Field

We begin with the field E^t transmitted into the dielectric layer $\zeta(x) < z < 0$. Fig. 10 displays the field intensity plot in the dielectric layer within the unit cell, computed via (16), for $n_h = 15$, $\theta^i = 15°$, and two different frequencies. In the HF case [$a/\lambda_0 = 6$, Fig. 10(a)], a fairly *complex/irregular* behavior is observed which visually resembles those of ergodic eigenfunctions in strongly chaotic billiards [59]. Moreover, there was found to be a strong sensitivity with respect to the incidence angle. Conversely, at lower frequencies [$a/\lambda_0 = 0.5$, Fig. 10(b)], the field intensity pattern exhibits more regular features. Similar regular behavior was observed in the presence of weaker refractive index gradients and shallower corrugations.

The above-noted visual resemblance between the HF field distribution in Fig. 10(a) and those of ergodic eigenfunctions in strongly chaotic billiards [59] suggests that RPW-type models [56] could be applicable to our configuration as well. To explore this possibility, we carried out a comprehensive statistical analysis of the HF transmitted field distribution. Fig. 11 shows the CDF of the field (magnitude) distributions in Fig. 10(a) ($a/\lambda_0 = 6$), over a spatial domain chosen according to the guidelines in Section V-A. As one can see, the CDF is nicely fitted by the RPW prediction (Rayleigh CDF [57]). Also shown in Fig. 11(a), for comparison, is the transmitted field CDF for a parameter configuration with $\Delta = 0$ (i.e., flat conducting surface) and the same electrical size, which *does not* exhibit ray chaos. In this case, the agreement with the corresponding Rayleigh fit is considerably poorer. This is better quantified in

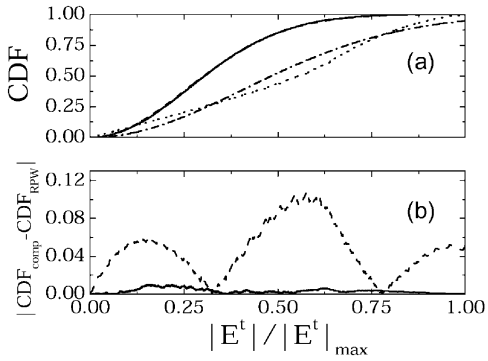

Fig. 11. As in Fig. 9, with $a/\lambda_0 = 6$. CDF of transmitted-field normalized amplitude $|E^t|/|E^t|_{\max}$ for undulating ($\Delta/a = 2/(5\pi)$) and flat ($\Delta = 0$) conducting surface. CDFs are estimated over a square observation domain of width $a/3$ centered at $(x_o = a/2, z_o = -h/2)$ and are compared with the RPW prediction (Rayleigh fit). (a) — Computed CDF (undulating surface); --- computed CDF (flat surface); …… Rayleigh fit (undulating surface); - · - · - Rayleigh fit (flat surface). (b) Absolute difference between computed CDF and RPW prediction. — Undulating surface; --- flat surface.

Fig. 11(b), where the absolute differences between the computed CDF and the corresponding Rayleigh fit are displayed for both cases. Slight variations in the agreement, as well as in the fit parameters, were observed for both cases when moving the observation domain across the unit cell.

Concerning the field spatial correlation, in 2-D ray-chaotic *homogeneous* billiards (e.g., Sinai or stadium), the RPW model predicts a Bessel J_0 behavior [56]

$$C(\mathbf{r}') \equiv \frac{\int\int_{\mathcal{D}} E\left(\mathbf{r} - \frac{\mathbf{r}'}{2}\right) E^*\left(\mathbf{r} + \frac{\mathbf{r}'}{2}\right) d\mathbf{r}}{\int\int_{\mathcal{D}} |E(\mathbf{r})|^2 d\mathbf{r}} \sim J_0(\kappa|\mathbf{r}'|) \quad (40)$$

where $\mathbf{r} \equiv (x, z)$, $\mathbf{r}' \equiv (x', z')$, * indicates complex conjugation and $\mathcal{D}$ is the observation domain (see the discussion in Section V-A). Note that in the above-mentioned ray-chaotic homogeneous billiards, the analysis is typically focused on modal wavefields, and κ in (40) corresponds to the modal wavenumber. Generalization of (40) to *inhomogeneous* configurations like ours is not straightforward. Nevertheless, we verified that (40) describes quite accurately the HF spatial correlation in the x'-direction at fixed z', via replacement of κ with an *effective* wavenumber κ_e obtained by curve fitting as noted below. Typical results are shown in Fig. 12. Specifically, for the HF field distribution in Fig. 10(a) $(a/\lambda_0 = 6)$, Fig. 12(a) shows an x'-cut (at $z' = 0$) of the real part of the spatial correlation computed numerically over a square observation domain of width $a/3$ centered at $(x_o = a/2, z_o = -h/2)$ versus its zeroth-order Bessel function (J_0) fit. Acceptable qualitative agreement is observed. The imaginary part of the numerically computed spatial correlation (not shown) was found to be practically negligible ($\lesssim$0.1 in absolute value). From the J_0-fit, we estimated the *effective* wavenumber κ_e in (40) numerically (in this example, $\kappa_e a \approx 62.13$). Repeating the experiment at different positions (x_o, z_o) of the observation domain center, the effective wavenumber was found to be dependent on z_o, as shown in Fig. 12(b). Also shown in Fig. 12(b), as a reference, is the behavior of the local wavenumber $k(z_o) = k_0 n(z_o)$. It is observed that, though not coincident, the effective and local wavenumbers exhibit the same trend.

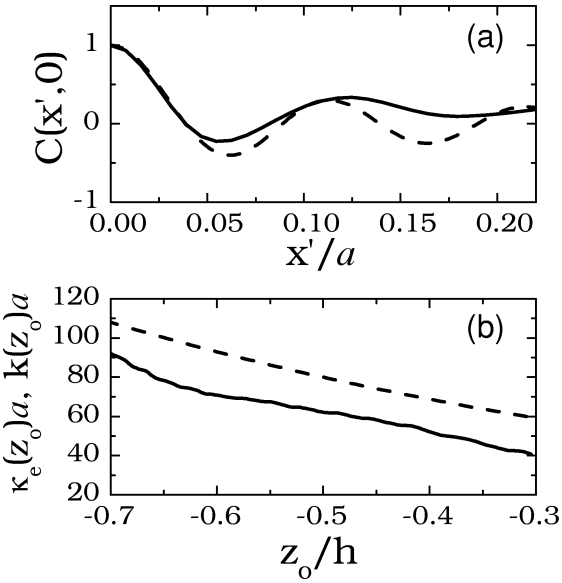

Fig. 12. As in Fig. 11, but spatial correlation in (40). (a) x'-cut at $z' = 0$. — Numerically computed over a square observation domain of width $a/3$ centered at $(x_o = a/2, z_o = -h/2)$; - - - zeroth-order Bessel function (J_0) fit. (b) Effective and local wavenumbers (scaled by unit cell size a) versus z_c/h. — Effective wavenumber $\kappa_e(z_o)$ in (40) estimated from J_0-fit; --- local wavenumber $k(z_o) = k_0 n(z_o)$.

The above results seem to confirm the anticipated tendency in the full-wave dynamics toward irregular behavior as the frequency of operation is increased. The field statistics in the irregular regime turn out to be consistent with those predicted by standard random-wave models.

C. Our Test Problem: Reflected Field

The far-field reflection properties of our configuration are embedded in the vector $\mathbf{b} \equiv [b_{m_i}, \ldots, b_{m_f}]$ of modal coefficients b_m in (15) corresponding to propagating Floquet modes (with m_i and m_f tagging the edges of the visible range). We have accordingly performed a comprehensive parametric analysis to reveal possible ray-chaotic footprints. For the same HF configuration as in Fig. 10(a), the real and imaginary parts of the Floquet-mode coefficients are shown in Fig. 13(a) and (b), for two slightly different incidence angles, with the subscript m identifying the Floquet-mode wavevector directions

$$\theta_m = \arcsin\left(\sin\theta^i - \frac{m\lambda_0}{a}\right). \quad (41)$$

One observes *strong* sensitivity of the field with respect to the incidence angle. This sensitivity was found to decrease substantially in the presence of weaker refractive index gradients [see, e.g., Fig. 13(c) and (d)], as well as shallower corrugations and lower frequencies. In order to parameterize such sensitivity in a compact and effective fashion, we consider the indicator

$$R_b \equiv \left|1 - \frac{\langle \mathbf{b}(\theta^i), \mathbf{b}(\theta^i + \Delta\theta^i)\rangle}{\|\mathbf{b}(\theta^i)\|^2}\right| = \left|1 - \frac{\sum_{m=m_i}^{m_f} b_m(\theta^i) b_m^*(\theta^i + \Delta\theta^i)}{\sum_{m=m_i}^{m_f} |b_m(\theta^i)|^2}\right| \quad (42)$$

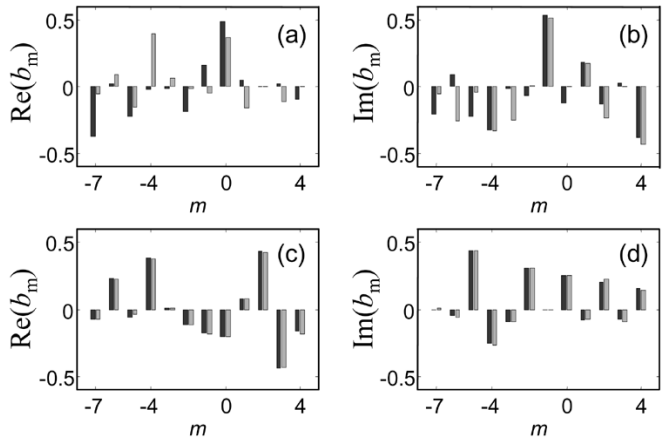

Fig. 13. Parameters as in Fig. 10, with $a/\lambda_0 = 6$. Real and imaginary parts of Floquet modal (reflection) coefficients b_m in (15), for two slightly different incidence angles, and two values of n_h. (a), (b) $n_h = 15$; (c), (d) $n_h = 1.05$. Dark shading: $\theta^i = 15°$; light shading: $\theta^i = 16°$.

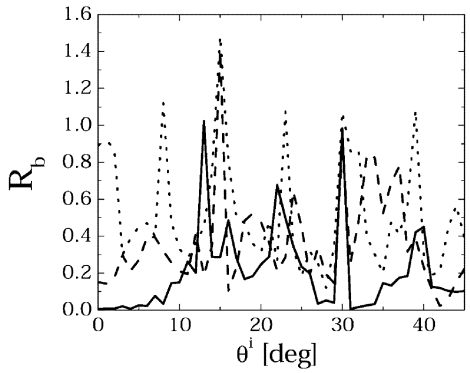

Fig. 14. As in Fig. 13, but with $n_h = 15$ only. Sensitivity indicator R_b in (42) (with $\Delta\theta^i = 1°$) versus incidence angle θ^i for different values of the electrical size a/λ_0. — $a/\lambda_0 = 1$; --- $a/\lambda_0 = 2$; ..... $a/\lambda_0 = 4$.

where the variation $\Delta\theta^i$ in the incidence angle is assumed to be sufficiently small so as not to appreciably change the Floquet modal structure [which depends on θ^i via (17)]. The indicator R_b in (42) corresponds to the distance in the complex plane between one and the normalized scalar product of two Floquet-coefficient vectors. Recalling the properties of the scalar product, it is readily verified that values of R_b close to zero indicate slight sensitivity (i.e., regular behavior) in the reflected field, and vice versa. For the same configurations as in Fig. 13 (with $n_h = 15$), the behavior of R_b within the angular interval $\theta^i \in [0, 45°]$ (with $\Delta\theta^i = 1°$) is displayed in Fig. 14, for three different values of the electrical size a/λ_0; the corresponding mean and variance (with respect to θ^i) are summarized in Table I. A rather spiky overall behavior is observed. Recalling that small values of R_b indicate slight sensitivity (i.e., smooth dependence on the incidence angle) in the reflected field, and vice versa, one can define "regular" regions as those where R_b remains sufficiently small. Such "regular" regions are clearly visible at lower frequencies $(a/\lambda_0 = 1)$ and progressively disappear at higher frequencies $(a/\lambda_0 = 2, 4)$, thereby indicating *overall larger sensitivity* of the reflection signatures with respect to the incidence angle. It is observed from Table I that both the mean and variance increase monotonically with increases in the electrical size.

TABLE I
MEAN VALUE AND VARIANCE (WITH RESPECT TO THE INCIDENCE ANGLE θ^i) OF THE SENSITIVITY INDICATOR R_b IN (42) FOR THE THREE CONFIGURATIONS IN FIG. 14. STATISTICS ARE ESTIMATED NUMERICALLY, USING 46 SAMPLES DISTRIBUTED UNIFORMLY WITHIN THE ANGULAR INTERVAL $\theta^i \in [0, 45°]$, WITH $\Delta\theta^i = 1°$

a/λ_0	Mean(R_b)	Variance(R_b)
1	0.214	0.232
2	0.375	0.264
4	0.506	0.303

Again, the above results seem to indicate a tendency, in the HF regime, toward irregular, random-like behavior of the reflection signatures, similar to those observed in open chaotic billiards [20], [21] and also in real-world complex scatterers [55].

D. Potential Applications

Besides its inherent academic interest, the ray-chaos-resembling wave dynamics exhibited by the test configuration presented here might be of interest in several EM engineering applications. For instance, the complex and extremely sensitive scattering signatures observed in Section V-C might be of potential use for radar countermeasures. We note that the combined effect of periodic corrugations and dielectric fillings has already been explored as a possible model for radar-cross-section reduction and control (see [66]). For such applications, ray chaos might offer new perspectives. In this connection, whole classes of ray-chaotic scatterers may be envisaged, based on known gravitational billiards, by replacing gravity with a suitably graded refractive index.

VI. CONCLUSIONS AND OPEN ISSUES

A novel class of ray-chaotic 2-D boundary-value problems has been shown to be associated with a particular novel synthetic test environment that involves both spatially confined and exterior-penetrating rays and modes. Ray-tracing simulations have been presented to illustrate its relevant ray-chaotic features. A rigorous full-wave analysis of the corresponding (TE-incidence) EM boundary value problem has been detailed and utilized to perform a comprehensive parametric study. Results for the high-frequency wave dynamics confirm the anticipated trends toward irregularity and other peculiar characteristics (not observed in geometries with "regular" ray behavior), which can be interpreted as "ray-chaotic footprints." In the irregular (random-like, ergodic) regime, the wave dynamics turns out to be effectively described by random-wave statistical models. Apart from the inherent academic interest, the test configuration here gives rise to performance characteristics that might be relevant, for example, to radar countermeasures.

Current and future research will be focused on still open issues, using the full-wave solution for our model as a synthetic testbed for calibration of asymptotic and other phenomenologically motivated parametric excursions. Thus, the full-wave approach, though rigorous and capable of producing essential reference solutions, does not provide a *direct* parameterization of the interaction between the ducted-type and the Floquet-type modes, which we hope to develop from a problem-matched

(high-frequency) asymptotic analysis. In this framework, hybrid ray-mode representations [44], as well as local spectral analysis [67], could be useful and insight-providing tools. Conformal mapping procedures (see [68]) that smooth out the periodicity of the undulating surface at the expense of additional inhomogeneities in the refracting index profile of (1) could be of potential interest for a different class of test environments. Other interesting and worthwhile issues pertain to the development of new random-wave statistical models for the irregular regime, tailored to our specific configuration. In this connection, random superpositions of solutions of the eikonal equation pertaining to the profile in (1), as well as the connection between the dwell-time distribution and the statistical correlation of the reflected wavefield [20], will be given attention.

ACKNOWLEDGMENT

The authors acknowledge stimulating discussions with Dr. A. Mackay (Q-Par Angus Ltd., UK), as well as the helpful comments provided by the reviewers.

REFERENCES

[1] H. Poincaré, *Les Methodes Nouvelles de laMecanique Celeste*. Paris, France: Gauthier-Villars, 1892.
[2] A. N. Kolmorogov, "Preservation of conditionally periodic movements with small change in the Hamiltonian function," *Dokl. Acad. Nauk SSSR*, vol. 98, pp. 527–530, 1954.
[3] ——, "A new metric invariant of transitive dynamical systems and automorphisms in Lebesgue spaces," *Dokl. Acad. Nauk SSSR*, vol. 119, pp. 861–864, 1958.
[4] Y. G. Sinai, "On the concept of entropy of a dynamical system," *Dokl. Acad. Nauk SSSR*, vol. 124, pp. 768–771, 1959.
[5] V. I. Arnold, "Small denominators and problems of stability of motion in classical and celestial mechanics," *Russ. Math. Surv.*, vol. 18, pp. 85–192, 1963.
[6] "Special issue on chaotic systems," *Proc. IEEE*, vol. 75, no. 8, Aug. 1987.
[7] Nonlinear Dynamics Group, Johannes Gutenberg Univ. Mainz, Germany. [Online]. Available: www.uni-mainz.de/FB/Physik/Chaos/chaosbib.html
[8] E. Ott, "Strange attractors and chaotic motions of dynamical systems," *Rev. Mod. Phys.*, vol. 53, no. 4, pp. 655–671, Oct. 1981.
[9] A. J. Lichtenberg and M. A. Liebermann, *Regular and Stochastic Motion*. New York: Springer-Verlag, 1983.
[10] C. Grebogi, E. Ott, and J. A. Yorke, "Chaos, strange attractors and fractal basin boundaries in nonlinear dynamics," *Sci.*, vol. 238, no. 4827, pp. 632–638, Oct. 1987.
[11] L. O. Chua and S. Parker, "Chaos: A tutorial for engineers," *Proc. IEEE*, vol. 75, pp. 982–1008, Aug. 1987.
[12] E. Ott, *Chaos in Dynamical Systems*. Cambridge, U.K.: Cambridge Univ. Press, 1993.
[13] R. C. Hilborn, *Chaos and Nonlinear Dynamics: An Introduction for Scientists and Engineers*. Oxford, U.K.: Oxford Univ. Press, 1994.
[14] I. M. Pinto, "Electromagnetic chaos: A tutorial," in *Proc. 8th Int. Conf. Electromagnetics in Advanced Applications (ICEAA '03)*, Torino, Italy, Sep. 8–12, 2003, pp. 511–514.
[15] T. Matsumoto, L. O. Chua, and M. Komuro, "The double scroll," *IEEE Trans. Circuits Syst.*, vol. CAS-32, pp. 797–818, Aug. 1985.
[16] N. B. Abraham, E. Arimondo, and R. W. Boyd, "Instabilities, dynamics and chaos in nonlinear optical systems," in *Instability and Chaos in Quantum Optics*, N. B. Abraham, F. T. Arecchi, and L. A. Lugiato, Eds. New York: Plenum, 1988, vol. NATO-ASI B177, pp. 375–391.
[17] V. Pierro and I. M. Pinto, "Radiation pressure induced chaos in multipendular Fabry Perot resonators," *Phys. Lett. A*, vol. 185, no. 1, pp. 14–22, Jan. 1994.
[18] Y. G. Sinai, "Dynamical systems with elastic reflections," *Russ. Math. Surv.*, vol. 25, no. 2, pp. 137–189, 1970.
[19] L. A. Bunimovich, "Conditions of stochasticity of two-dimensional billiards," *Chaos*, vol. 1, no. 2, pp. 187–193, Aug. 1991.
[20] T. Kottos, U. Smilansky, J. Fortuny, and G. Nesti, "Chaotic scattering of microwaves," *Radio Sci.*, vol. 34, no. 4, pp. 747–758, Jul.–Aug. 1999.
[21] A. Wirzba, "Quantum mechanics and semiclassics of hyperbolic n-disk scattering systems," *Phys. Rep.*, vol. 309, no. 1–2, pp. 1–116, Feb. 1999.
[22] M. V. Berry, "Quantum chaology," *Proc. Roy. Soc. London*, vol. A413, pp. 183–198, 1987.
[23] M. Tabor, *Chaos and Integrability in Nonlinear Dynamics*. New York: Wiley, 1989.
[24] M. C. Gutzwiller, *Chaos in Classical and Quantum Mechanics*. New York: Springer-Verlag, 1990.
[25] F. Haake, *Quantum Signatures of Chaos*. New York: Springer, 1991.
[26] A. J. Mackay, "Application of chaos theory to ray tracing in ducts," *Proc. Inst. Elect. Eng. Radar, Sonar Nav.*, vol. 164, no. 6, pp. 298–304, Dec. 1999.
[27] ——, "An application of chaos theory to the high frequency RCS prediction of engine ducts," in *Ultra-Wideband, Short-Pulse Electromagnetics 5*, P. D. Smith and S. R. Cloude, Eds. New York: Kluwer/Academic, 2002, pp. 723–730.
[28] ——, "Calculating the radar cross section of electrically large ducts using random waves and rays," in *Proc. 8th Int. Conf. Electromagnetics in Advanced Applications (ICEAA '03)*, Torino, Italy, Sep. 8–12, 2003, pp. 515–518.
[29] L. Cappetta, M. Feo, V. Fiumara, V. Pierro, and I. M. Pinto, "Electromagnetic chaos in mode stirred reverberation enclosures," *IEEE Trans. Electromagn. Compat.*, vol. 40, pp. 185–192, 1998.
[30] V. Fiumara, V. Galdi, V. Pierro, and I. M. Pinto, "From mode-stirred enclosures to electromagnetic Sinai billiards: Chaotic models of reverberation enclosures," in *Proc. 6th Int. Conf. Electromagnetics in Advanced Applications (ICEAA '99)*, Torino, Italy, Sep. 15–17, 1999, pp. 357–360.
[31] C. Gmachl, F. Capasso, E. E. Narimanov, J. U. Nockel, A. D. Stone, J. Faist, D. L. Sivco, and A. Y. Cho, "High-power directional emission from microlasers with chaotic resonators," *Science*, vol. 280, no. 5369, pp. 1556–1564, Jun. 1998.
[32] P. B. Wilkinson, T. M. Fromhold, R. P. Taylor, and A. P. Micolich, "Electromagnetic wave chaos in gradient refractive index optical cavities," *Phys. Rev. Lett.*, vol. 86, no. 24, pp. 5466–5469, Jun. 2001.
[33] R. R. Parwani. Complexity. [Online]. Available: http://staff.science.nu.edu/~parwani/complexity
[34] V. Fiumara, V. Galdi, V. Pierro, and I. M. Pinto, "Bouncing ray chaos for smart media," in *Proc.IEEE Antennas Propag. Int. Symp.*, Salt Lake City, UT, Jul. 16–21, 2000, pp. 682–684.
[35] T. Harayama and P. Gaspard, "Diffusion of particles bouncing on a one-dimensional periodically corrugated floor," *Phys. Rev. E*, vol. 64, no. 036 215, Aug. 2001.
[36] M. Born and E. Wolf, *Principles of Optics*. New York: Pergamon, 1993.
[37] W. H. Press, S. A. Teukolsky, W. T. Vetterling, and B. P. Flannery, *Numerical Recipes in C: The Art of Scientific Computing*, 2nd ed. Cambridge, U.K.: Cambridge Univ. Press, 1992.
[38] M. Eichengrün, W. Schirmacher, and W. Breymann, "Qua ntum manifestations of chaotic scattering in the presence of KAM tori," *Europhys. Letts.*, vol. 36, no. 7, pp. 483–489, Dec. 1996.
[39] S. M. Hammel, J. A. Yorke, and C. Grebogi, "Do numerical orbits of chaotic dynamical processes represent true orbits?," *J. Complexity*, vol. 3, no. 2, pp. 136–145, 1987.
[40] M. K. Moaveni, "Plane wave diffraction by dielectric gratings, finite-difference formulation," *IEEE Trans. Antennas Propag.*, vol. 37, no. 8, pp. 1026–1031, Aug. 1989.
[41] J.-F. Kiang, "Backscattering of TE waves by periodical surface with dielectric cover," *IEEE Trans. Antennas Propag.*, vol. 46, pp. 176–180, Feb. 1998.
[42] M. Abramowitz and I. E. Stegun, *Handbook of Mathematical Functions*. New York: Dover, 1972.
[43] A. P. Prudnikov, Y. A. Brychkov, and O. I. Marichev, *Integrals and Series*. New York: Gordon and Breach, 1986.
[44] L. B. Felsen, "Progressing and oscillatory waves for hybrid synthesis of source excited propagation and diffraction," *IEEE Trans. Antennas Propag.*, vol. AP-32, no. 8, pp. 775–796, Aug. 1984.
[45] G. H. Golub and C. F. Van Loan, *Matrix Computations*, 3rd ed. Baltimore, MD: John Hopkins Univ. Press, 1996.
[46] S. Wolfram, *The Mathematica Book*. Cambridge, U.K.: Cambridge Univ. Press, 1999.

[47] O. Bohigas, M. J. Giannoni, and C. Schmit, "Characterization of chaotic quantum spectra and universality of level fluctuation laws," *Phys. Rev. Lett.*, vol. 52, no. 1, pp. 1–4, Jan. 1984.
[48] M. V. Berry, "Semiclassical theory of spectral rigidity," *Proc. Roy. Soc. London*, vol. A400, pp. 229–251, 1985.
[49] M. L. Mehta, *Random Matrices*. New York: Academic, 1967.
[50] G. Blum, S. Gnutzmann, and U. Smilansky, "Nodal domain statistics: A criterion for quantum chaos," *Phys. Rev. Lett.*, vol. 88, no. 114 101, Mar. 2002.
[51] A. Peres, "Stability of quantum motion in chaotic and regular systems," *Phys. Rev. A*, vol. 30, no. 4, pp. 1610–1615, Oct. 1984.
[52] C. Draeger and M. Fink, "One-channel time reversal of elastic waves in a chaotic 2D-silicon cavity," *Phys. Rev. Lett.*, vol. 79, no. 3, pp. 407–410, Jul. 1997.
[53] R. A. Jalabert and H. M. Pastawski, "Environment-independent decoherence rate in classically chaotic systems," *Phys. Rev. Lett.*, vol. 86, no. 12, pp. 2490–2493, Mar. 2001.
[54] E. J. Heller, "Bound-state eigenfunctions of classically chaotic Hamiltonian systems: Scars of periodic orbits," *Phys. Rev. Lett.*, vol. 53, no. 16, pp. 1515–1518, Oct. 1984.
[55] E. K. Miller and T. K. Sarkar, "Model-order reduction in electromagnetics using model-based parameter estimation," in *Frontiers in Electromagnetics*, D. H. Werner and R. Mittra, Eds. Piscataway, NJ: IEEE Press, 1999, ch. 9, pp. 371–436.
[56] M. V. Berry, "Regular and irregular semiclassical wavefunctions," *J. Phys. A: Math. Gen.*, vol. 10, pp. 2083–2091, 1977.
[57] A. Abdi, H. Hashemi, and S. Nader-Esfahani, "On the PDF of a sum of random vectors," *IEEE Trans. Commun.*, vol. 48, pp. 7–12, Jan. 2000.
[58] B. Eckhardt, U. Dörr, U. Kuhl, and H.-J. Stöckmann, "Correlations of electromagnetic fields in chaotic cavities," *Europhys. Lett.*, vol. 46, no. 2, pp. 134–140, Apr. 1999.
[59] S. W. McDonald and A. N. Kaufman, "Wave chaos in the stadium: Statistical properties of short-wave solutions of the Helmholtz equation," *Phys. Rev. A*, vol. 37, no. 8, pp. 3067–3086, Apr. 1988.
[60] H.-J. Stöckmann, "Microwave studies of chaotic billiards and disordered systems," *J. Mod. Opt.*, vol. 49, no. 12, pp. 2045–2059, Oct. 2002.
[61] D. A. Hill, "Plane-wave integral representation for fields in reverberation chambers," *IEEE Trans. Electromagn. Compat.*, vol. 40, pp. 209–217, Aug. 1998.
[62] D. A. Hill and J. M. Ladbury, "Spatial-correlation functions of fields and energy density in a reverberation chamber," *IEEE Trans. Electromagn. Compat.*, vol. 44, no. 2, pp. 95–101, Feb. 2002.
[63] A. Backer, J. P. Keating, and S. D. Prado, "Orbit bifurcations and wavefunction autocorrelations," *Nonlinearity*, vol. 15, no. 5, pp. 1417–1433, Sept. 2002.
[64] M. V. Berry, J. P. Keating, and H. Schomerus, "Universal twinkling exponents for spectral fluctuations associated with mixed chalogy," *Proc. Roy. Soc. London A*, vol. 456, pp. 1659–1668, 2000.
[65] A. Backer and R. Schubert, "Autocorrelation function of eigenstates in chaotic and mixed systems," *J. Phys. A: Math. Gen.*, vol. 35, no. 3, pp. 539–564, Jan. 2002.
[66] J.-F. Kiang, "Scattering properties of circular cylinders with periodical corrugations in the azimuthal direction," *IEEE Trans. Antennas Propag.*, vol. 46, no. 10, pp. 1589–1590, Oct. 1998.
[67] L. Carin and L. B. Felsen, "Wave-oriented data processing for frequency and time domain scattering by nonuniform truncated arrays," *IEEE Antennas Propag. Mag.*, vol. 36, pp. 29–43, Jun. 1994.
[68] M. Neviere, M. Cadilhac, and R. Petit, "Applications of conformal mappings to the diffraction of electromagnetic waves by a grating," *IEEE Trans. Antennas Propag.*, vol. AP-21, no. 1, pp. 37–46, Jan. 1973.

Giuseppe Castaldi was born in Benevento, Italy, in 1968. He received the Laurea degree *(summa cum laude)* in electrical engineering from the "Federico II" University of Naples, Italy, in 1995 and the Ph.D. degree in applied electromagnetics from the University of Salerno, Italy, in 1999.

In 2001, he was a Postdoctoral Research Fellow at the TNO Physics and Electronics Laboratory, The Hague, The Netherlands. In 2003, he became an Assistant Professor of electromagnetics at the Department of Engineering, University of Sannio, Benevento, Italy. His research interests include electromagnetic chaos, quasi-periodic antenna arrays, applications of neural networks to inverse scattering problems, and field representations in complex environments.

Vincenzo Fiumara was born in Salerno, Italy. He received the Laurea degree *(summa cum laude)* in electrical engineering and the Ph.D. degree in applied electromagnetics from the University of Salerno, Italy, in 1993 and 1997, respectively.

In 1993, he joined the Electromagnetic and Gravitational Wave Group, University of Salerno. He became an Assistant Professor of electromagnetics in 1999. He has been teaching electromagnetics and microwaves at the University of Salerno since then. His current research interests include complexity and nonlinearity in electromagnetics, and microwave power applications.

Dr. Fiumara received an Italian National Research Council fellowship in 1998.

Vincenzo Galdi (M'98–SM'04) was born in Salerno, Italy, on July 28, 1970. He received the Laurea degree *(summa cum laude)* in electrical engineering and the Ph.D. degree in applied electromagnetics from the University of Salerno in 1995 and 1999, respectively.

From April to December 1997, he held a visiting position in the Radio Frequency Division of the European Space Research and Technology Centre (ESTEC-ESA), Noordwijk, The Netherlands. From September 1999 to August 2002, he was a Research Associate in the Department of Electrical and Computer Engineering, Boston University, Boston, MA. In November 2002, he became an Associate Professor of electromagnetics at the Department of Engineering, University of Sannio, Benevento, Italy. His research interests include analytical and numerical techniques for wave propagation in complex environments, electromagnetic chaos, and inverse scattering.

Dr. Galdi is a member of Sigma Xi. He received a 2001 International Union of Radio Science Young Scientist Award.

Vincenzo Pierro was born in Salerno, Italy, in 1967. He received the Laurea degree *(summa cum laude)* in physics from the University of Salerno in 1990.

In 1991, he held a visiting position in the COLUMBUS Metrology Group at the European Space Research and Technology Centre (ESTEC-ESA), Noordwijk, The Netherlands. Since 1996, he has been with the Faculty of Engineering, University of Sannio, Benevento, Italy, where he became Assistant Professor of electromagnetics in 1996 and Associate Professor in 2001. In 1999, he received a research fellowship from the Japan Society for the Promotion of Science in connection with the TAMA 300 experiment. His main research interests are in the field of complex electromagnetic systems, electromagnetic detection of gravitational waves, and applied mathematics.

Dr. Pierro is a member of the Italian Physical Society.

Innocenzo M. Pinto (M'99) was born and educated in Italy.

Winner of national competitions, he was appointed Assistant Professor of electromagnetics in 1983, Associate Professor in 1987, and full Professor in 1990. He has been a Faculty Member of the Universities of Naples, Salerno (where he founded and chaired the Ph.D. program in Information Engineering from 1993 to 2001), Catania, and Sannio at Benevento, where he is currently the Dean of the Information Engineering Curricula Committee. He has visited several research institutions as an invited Lecturer, including CERN, KEK, and NIST (formerly NBS). In 1998, he was a European Union Senior Visiting Scientist at the National Astronomical Observatory, Tokyo, Japan, in connection with TAMA300 experiment. He has authored or co-authored more than 100 technical papers in peer-reviewed international journals. His research interest span from electrophysics to gravitational wave experiments.

Prof. Pinto is a Member of the American Physical Society.

Leopold B. Felsen (S'47–M'54–SM'55–F'62–LF'90) was born in Munich, Germany, on May 7, 1924. He received the B.E.E., M.E.E, and D.E.E. degrees from the Polytechnic Institute of Brooklyn, Brooklyn, NY, in 1948, 1950, and 1952, respectively.

He emigrated to the United States in 1939 and served in the U.S. Army from 1943 to 1946. After 1952 he remained with the Polytechnic (now Polytechnic University), becoming University Professor in 1978. From 1974 to 1978 he was Dean of Engineering. In 1994 he resigned from the full-time Polytechnic faculty and was granted the status of University Professor Emeritus. He is now Professor of aerospace and mechanical engineering and Professor of electrical and computer engineering at Boston University, Boston, MA (part-time). He is the author or coauthor of more than 350 papers and of several books, including *Radiation and Scattering of Waves* (Piscataway, NJ: IEEE Press, 1994). He is an Associate Editor of several professional journals and was an Editor of the Wave Phenomena Series (New York: Springer-Verlag). His research interests encompass wave propagation and diffraction in complex environments and in various disciplines, high-frequency asymptotic and short-pulse techniques, and phase-space methods with an emphasis on wave-oriented data processing and imaging.

Dr. Felsen is a Member of Sigma Xi and a Fellow of the Optical Society of America and the Acoustical Society of America. He has held named Visiting Professorships and Fellowships at universities in the United States and abroad, including the Guggenheim in 1973 and the Humboldt Foundation Senior Scientist Award in 1981. In 1974 he was an IEEE Antennas and Propagation Society (APS) Distinguished Lecturer. His "Poet's Corner" appears sporadically in the IEEE/APS Magazine. He received the IEEE/APS Best Paper Award for 1969 and was best paper co-author for 1974 and 1981. He was a contributing author to papers selected for the R. W. P. King Award for 1984, 1986, and 2000. He received the Balthasar van der Pol Gold Medal from the International Union of Radio Science (URSI) in 1975, an Honorary Doctorate from the Technical University of Denmark in 1979, the IEEE Heinrich Hertz Gold Medal for 1991, the APS Distinguished Achievement Award for 1998, the IEEE Third Millennium Medal in 2000, an honorary Laurea degree from the University of Sannio in Benevento, Italy in 2003, the IEEE Electromagnetics Award for 2003, an honorary doctorate from the Technical University of Munich, Germany in 2004, three Distinguished Faculty Alumnus Awards from Polytechnic University, and an IEEE Centennial Medal in 1984. In 1977, he was elected to the National Academy of Engineering. He served on the APS Administrative Committee from 1963 to 1966 and was Vice Chairman and Chairman for both the US (1966–1973) and the International (1978–1984) URSI Commission B.